Journal of Materials Chemistry A

ROYAL SOCIETY OF CHEMISTRY

PAPER

View Article Online
View Journal | View Issue

Open Access Article. Published on 24 April 2025. Downloaded on 5/17/2026 5:31:30 AM.
This article is licensed under a Creative Commons Attribution-NonCommercial 3.0 Unported Licence.

Check for updates

Cite this: J. Mater. Chem. A, 2025, 13, 17511

Dual-functional surface of MXene anodes boosts long-term cyclability of lithium-metal batteries†

Jeesoo Yoon,[a] Oh B. Chae,[b] Mihye Wu *[cd] and Hee-Tae Jung *[a]

Introducing seed elements with high lithiophilicity onto the anode is a promising strategy to mitigate dendrite growth in lithium metal batteries (LMBs). Two primary seed elements have been explored: (i) lithiophilic metals (*e.g.* Ag, Au, and Sn), and (ii) fluorine (−F) functionalities. Despite significant advancements, hybrid materials combining the two elements have not been realized. Moreover, it remains unclear which element enhances LMB performance more. In this study, we engineered, for the first time, a high-density dual-functional surface incorporating lithiophilic metals and −F functionalities. Through rapid Joule heating, we integrated high-density Au nanoparticles (Au NPs) onto the F-terminated $Ti_3C_2T_x$ MXene anode surface. Our findings reveal distinct roles for each element: Au NPs reduce the size of deposited lithium, while −F functionalities promote uniform lithium distribution with a LiF-rich solid electrolyte interphase (SEI) layer. Notably, the synergistic effect of Au NPs and −F functionalities extended the lifespan of Au@F-rich $Ti_3C_2T_x$ to 600 cycles compared to the initial 100 cycles of $Ti_3C_2T_x$ and 240 cycles of Au@$Ti_3C_2T_x$. These results underscore the pivotal role of −F functionalities in prolonging and enhancing the performance of LMBs. This research highlights the importance of tailored surface functionalities and offers a promising pathway for the design of advanced LMB components.

Received 19th January 2025
Accepted 22nd April 2025

DOI: 10.1039/d5ta00519a

rsc.li/materials-a

Introduction

Lithium-metal batteries (LMBs) are considered one of the most promising candidates for next-generation energy storage devices, owing to their high theoretical capacity (3860 mA h g^{-1}) and low negative electrode potential (−3.04 V *vs.* the standard hydrogen electrode).[1,2] However, their practical application is impeded by the uncontrolled growth of lithium dendrites during charge/discharge cycles, which can cause internal short circuits and safety hazards.[3–5] Various approaches have been explored to address this issue, including electrolyte composition adjustments,[6,7] artificial solid electrolyte interphase (SEI) coating layers,[8] physical protective barriers,[9] separator modifications,[10] and anode substrate structural designs.[11]

Among these, enhancing lithiophilicity on the anode substrate stands out as particularly effective in promoting uniform lithium deposition and suppressing dendrite formation. This approach aims to create a favorable environment for uniform Li nucleation and growth, thereby minimizing the formation of dendritic structures. Numerous lithiophilic seeds have been explored in previous studies. In particular, introducing seed elements on the anode can effectively reduce the Li nucleation overpotential. Metals and metal oxides, including Au,[12] Ag,[13] Zn,[14] Sn,[15] Cu_2O[16] and ZnO,[17] are well-known seed materials. The energy barrier for Li nucleation can be lowered or neglected in their presence due to the reduced thermodynamic mismatch or strong interaction with lithium.[18,19] Thus, Li deposition, including both Li nucleation and subsequent deposition, can be effectively regulated by seed materials, which determines the electrochemical performance of the Li metal battery. Among these, enhancing lithiophilicity on the anode substrate stands out as particularly effective in promoting uniform lithium deposition and suppressing dendrite formation. This strategy creates an environment conducive to uniform lithium nucleation, minimizing dendritic growth.

Generating seed elements with lithiophilic surface functionality is another crucial factor influencing the performance of Li-metal batteries, as it impacts both lithiophilicity and interphase control. In particular, the presence of fluorine (−F) functional groups on the anode surface plays a vital role in lithium-metal batteries.[20] These −F groups are essential in the

[a]National Laboratory for Organic Opto-electronic Materials, Department of Chemical and Biomolecular Engineering (BK-21 four), Korea Advanced Institute of Science and Technology (KAIST), Center for KAIST-UC Berkeley-VNU Global Climate Change, 291 Daehak-ro, Yuseong-gu, Daejeon, Korea. E-mail: heetae@kaist.ac.kr

[b]School of Chemical, Biological and Battery Engineering, Gachon University, Seongnam-si, Gyeonggi-do 13120, Republic of Korea

[c]School of International Engineering and Science, Jeonbuk National University, Jeonju-si, Jeonbuk State, 54896 Republic of Korea. E-mail: wumihye@jbnu.ac.kr

[d]Advanced Materials Division, Korea Research Institute of Chemical Technology, Yuseong-gu, Daejeon 34114, Korea

† Electronic supplementary information (ESI) available. See DOI: https://doi.org/10.1039/d5ta00519a

Open Access Article. Published on 24 April 2025. Downloaded on 5/17/2026 5:31:30 AM. This article is licensed under a Creative Commons Attribution-NonCommercial 3.0 Unported Licence.

formation and composition of the solid–electrolyte interphase (SEI) layer, which is a key component governing the battery's performance and safety characteristics. The presence of –F functionality on the anode surface promotes the formation of a LiF-rich SEI layer. LiF is a desirable component in the SEI layer because it exhibits several beneficial properties, such as high mechanical strength, high ionic conductivity, and chemical stability. By introducing –F functionality on the anode surface, such as through the use of fluorinated materials or surface coatings, the formation of a LiF-rich SEI layer is facilitated.[21] This LiF-rich SEI layer can effectively regulate lithium-ion flux, promoting uniform lithium deposition and suppressing dendrite growth, ultimately improving the cycle life, coulombic efficiency, and safety of lithium-metal batteries.

Building upon the previous discussion, it is evident that both lithiophilic metals and elements with fluorine functional groups play crucial roles in promoting uniform lithium deposition and suppressing dendrite growth in lithium-metal batteries. However, simultaneously achieving a uniform and high-density distribution of both metal seed particles and fluorine functional groups on the anode substrate surface has proven to be critically challenging. Furthermore, the relative importance of the metal seed particles *versus* the fluorine functional groups in promoting this desired uniformity and high density remains unclear. MXenes, a class of two-dimensional transition metal carbides, nitrides, or carbonitrides, emerge as promising candidates to address this challenge. Due to their unique structural and compositional features, MXenes offer the potential to simultaneously incorporate both metal seed sites and fluorine functionality on the anode substrate, thereby synergistically combining the benefits of both approaches.[22,23]

In this study, we designed a new surface structure with a dual-functional surface on the $Ti_3C_2T_x$ MXene anode by combining the benefits of F-terminated groups and Au nanoparticles (NPs), and evaluated the impact of surface termination and the incorporation of Au NPs on reactivity with lithium. The F-terminated groups contribute to the formation of a desirable LiF-rich SEI layer, which is the most critical factor in Li-metal battery performance as it stabilizes the lithium flux. Simultaneously, the Au NP seeds act as nucleation sites, guiding uniform lithium deposition. This synergistic combination of a stable LiF-rich SEI layer and uniform lithium nucleation sites provided by the F-termination and Au NPs, respectively, results in a significant enhancement in the long-term performance of Li metal batteries.

Experimental

Synthesis of $Ti_3C_2T_x$ MXene

$Ti_3C_2T_x$ MXene was synthesized by chemical wet-etching of its precursor Ti_3AlC_2 MAX phase following the MILD method from a previous protocol report. 0.8 g of LiF was added to 10 mL of 9 M HCl with continuous stirring for preparing the etchant. Then, 0.5 g of Ti_3AlC_2 MAX powder was gradually added to the etchant under continuous stirring over the course of 5 min. The resultant mixture was maintained at 35 °C for 24 h. The acidic reactant was washed with DI water by centrifugation (3500 rpm, 5 min per cycle) until the supernatant reached a pH level of ≈6. The single-layer $Ti_3C_2T_x$ MXene containing supernatant with a concentration of 10 mg mL^{-1} was used for further experiments.

Synthesis of F-rich $Ti_3C_2T_x$ MXene

F-Rich $Ti_3C_2T_x$ MXene was synthesized by using HF to prepare the etchant. 0.5 g of LiCl was added to 15 mL of acidic etchant containing 12 M HCl, DI water, and 28.4 M HF in a 2 : 2:1 volume ratio with continuous stirring. Then, 0.5 g of Ti_3AlC_2 MAX powder was gradually added to the etchant under continuous stirring over the course of 5 min. The resultant mixture was maintained at 35 °C for 8 h. The acidic reactant was washed with DI water by centrifugation (3500 rpm, 5 min per cycle) until the supernatant reached a pH level of ≈6. The single-layer $Ti_3C_2T_x$ MXene containing supernatant with a concentration of 10 mg mL^{-1} was used for further experiments.

Fabrication of $Ti_3C_2T_x$ MXene aerogel

5 mL of single-layer $Ti_3C_2T_x$ MXene solution (concentration of 10 mg mL^{-1}) was poured in a Petri dish with a diameter of 6 mm and placed inside a −80 °C freezer for 24 h. Then, the frozen sample was transferred to a −110 °C freeze-dryer to prepare the $Ti_3C_2T_x$ MXene aerogel.

Preparation of gold precursor solution

Gold(III) chloride hydrate was purchased from Sigma-Aldrich. Gold precursor solution was prepared by dissolving the gold(-III) chloride hydrate precursor in ethanol with a final concentration of 0.05 M.

Synthesis of Au@$Ti_3C_2T_x$ MXene by rapid Joule heating

The $Ti_3C_2T_x$ MXene aerogel was attached to quartz plate using copper tape and silver paste to prepare a freestanding MXene aerogel substrate. Following the preparation of the substrate, 100 μL of gold precursor solution was drop-coated on the substrate while heating at 80 °C. Once ethanol was evaporated, rapid heating was conducted with 1 A current for 100 ms under an Ar atmosphere for the synthesis of gold metal NPs on the MXene surface.

Characterization

Scanning electron microscopy (FEI, Magellan400) was used to observe MXene aerogel morphology and the synthesized metal NPs on the MXene surface at an accelerating voltage of 10 kV. Transmission electron microscopy (FEI, Talos F200X, Tecnai F20) was used at 200 kV to observe metal NP synthesis on the MXene surface. High-angle annular dark-field scanning TEM (HAADF-STEM) mode and energy-dispersive X-ray spectrometry were used to analyze lattice spacing and elemental distribution. XPS (Thermo VG Scientific, K-alpha) was performed with a monochromatic Al Kα (1486.6 eV) X-ray source to analyze the chemical states of the prepared samples.

Open Access Article. Published on 24 April 2025. Downloaded on 5/17/2026 5:31:30 AM.
This article is licensed under a Creative Commons Attribution-NonCommercial 3.0 Unported Licence.

Electrochemical measurements

Electrochemical measurements were performed using CR2032-type coin cells, which were fabricated in an argon-filled glovebox. The Li/Cu cells consisted of the prepared substrates, a polyethylene (PE) separator, and lithium metal. The electrolyte used was composed of 1 M lithium hexafluorophosphate ($LiPF_6$) dissolved in a mixture of ethylene carbonate (EC) and dimethyl carbonate (DMC) in a 1 : 1 volume ratio, with the addition of 10 wt% fluoroethylene carbonate (FEC) and 2 wt% vinylene carbonate (VC). The galvanostatic charge/discharge performance was measured using a battery cycler (WBCS-3000, WonAtech). Lithium deposition behavior was studied at a current density of 0.1 mA cm^{-2} with capacities of 0.1 and 1 mA h cm^{-2}. For cyclic stability testing, a current density of 1.0 mA cm^{-2} (with a capacity of 1.0 mA h cm^{-2}) was applied.

Results and discussion

Fig. 1 exhibits the overall scheme for fabricating a dual-functional surface on the $Ti_3C_2T_x$ MXene anode to combine the benefits of lithiophilic F-terminations and Au nanoseeds. We used MXenes as the lithium anode material in this study, as MXenes are known for their 2 dimensional nanostructure, high surface area, electrical conductivity and high availability of fluorine (–F) functional groups.[22,24] In addition, MXenes have shown great potential as lithium metal battery anodes by functioning as a buffer layer for Li volume expansion and as a host material.[8,25–27] In order to first synthesize a high density of fluorine termination on $Ti_3C_2T_x$ MXene, we prepared the $Ti_3C_2T_x$ MXene anode by chemical wet etching from the Ti_3AlC_2 MAX phase followed by freeze-drying (Fig. S1†).[28] $Ti_3C_2T_x$ MXene with different surface termination compositions was prepared by moderating the composition of the acid etchants. In fact, it is well-reported that the proportion of surface terminations, –F and –O, is highly dependent on the synthesis method.[29,30] To prepare F-rich $Ti_3C_2T_x$ MXene, the etchant was composed of mainly hydrofluoric (HF) acid, while the etchant to prepare normal $Ti_3C_2T_x$ MXene followed the minimally intensive layer delamination (MILD) treatment, containing only hydrochloric (HCl) acid with lithium fluoride. An increase in the proportion of HF in the etchant is known to significantly increase the amount of –F termination as the competition between metal ions is much less compared to using fluoride salts.[30] Successful synthesis of $Ti_3C_2T_x$ MXene using both etching parameters was confirmed by XRD, where the shift of the (002) peak from 9.5 degrees to a lower angle signifies the removal of Al from the Ti_3AlC_2 and the addition of surface terminations (Fig. S2†).[28] Both prepared MXenes were freeze-dried into aerogel morphologies to construct a highly porous 3-dimensional lithium host structure (Fig. S3†).

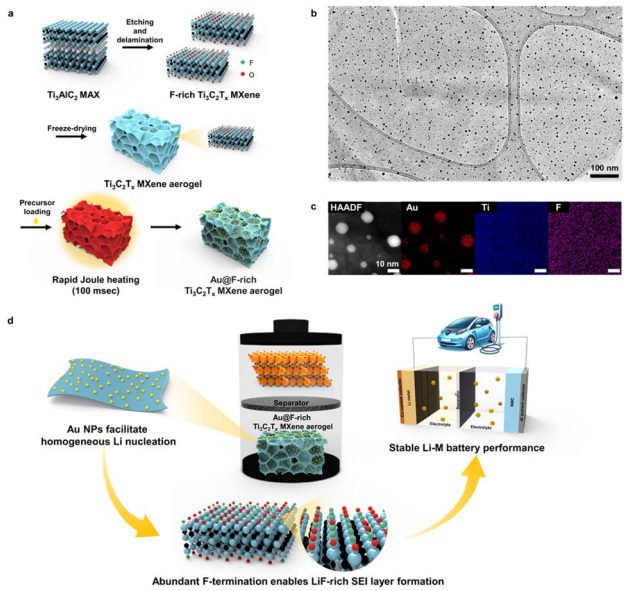

Fig. 1 Synthesis of Au NPs on surface termination controlled $Ti_3C_2T_x$ MXene by rapid Joule heating for Li-metal battery anodes. (a) Chemical wet etching and rapid Joule heating synthesis of Au@F-rich $Ti_3C_2T_x$ MXene. (b) TEM image and (c) TEM-EDS image of Au@F-rich $Ti_3C_2T_x$ MXene. (d) Schematic illustration of Au@F-rich $Ti_3C_2T_x$ MXene as a Li-metal battery anode.

To synthesize high-density Au NPs on the 3-dimensional MXene substrate, a 0.05 M Au precursor solution was drop-cast on the substrate and dried for 15 minutes prior to the heating process. Rapid Joule heating was then conducted by applying an electric pulse for a short duration of 100 milliseconds (Fig. S4†). Upon rapid Joule heating, Au NPs were uniformly synthesized on MXene aerogel, as illustrated in Fig. 1a. This process involves the generation of intense heat during the passage of electric current through the substrate for a very short time interval. Since $Ti_3C_2T_x$ MXene contains abundant surface termination groups which act as metal binding sites, dense formation of Au NPs is possible without significant aggregation.[31] In addition, it is noteworthy that this process minimizes MXene damage, preserves F-functionalities, and enables homogeneous Au NP distribution. Importantly, the absence of solution-based processing during metal NP formation helps to mitigate MXene oxidation during synthesis. Minimization of aqueous exposure suppresses TiO_2 formation on the MXene surface, allowing full utilization of MXene's lithiophilic qualities even after NP synthesis.[32]

Fig. 1b shows a representative transmission electron microscopy (TEM) image of Au@F-rich $Ti_3C_2T_x$ MXene. High density Au NPs were evenly distributed over large areas with a uniform size distribution. Such highly dense Au NPs were also fabricated on normal $Ti_3C_2T_x$ MXene with no apparent difference compared to F-rich samples, as they both contain a high level of surface terminations which can act as metal binding sites (Fig. S5†).[33,34] The successful synthesis of Au NPs and retained content of F-terminations were further verified through TEM-EDS, with minimized damage to the $Ti_3C_2T_x$ MXene surface (Fig. 1c). Also, this rapid Joule heating technique is a non-destructive method in which the MXene aerogel structure is well maintained even after the heating process (Fig. S6†). This non-destructive process allows direct utilization of the prepared material as lithium metal battery substrates without additional processing. The combined effects of homogeneously distributed lithiophilic seeds, abundant F-

Open Access Article. Published on 24 April 2025. Downloaded on 5/17/2026 5:31:30 AM.
This article is licensed under a Creative Commons Attribution-NonCommercial 3.0 Unported Licence.

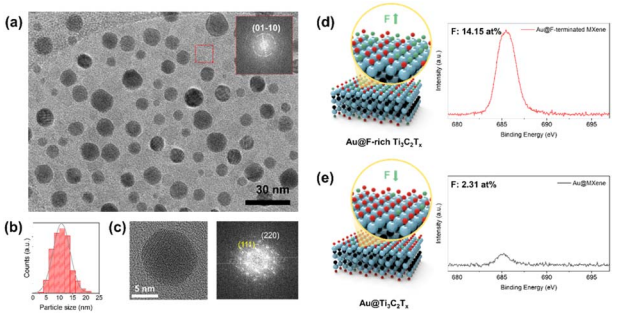

Fig. 2 Identification of the synthesized Au NPs on F-rich $Ti_3C_2T_x$ MXene and fluorine terminations. (a) TEM image of Au@F-rich $Ti_3C_2T_x$ MXene, (b) particle size distribution of Au NPs, (c) high resolution TEM (HRTEM) bright field image of Au NP and the corresponding FFT pattern. F 1s XPS spectra of (d) Au@F-rich $Ti_3C_2T_x$ and (e) as prepared Au@$Ti_3C_2T_x$ (before Li deposition).

terminations and the three-dimensional host structure provide long stability in Li-metal battery performance (Fig. 1d).[35]

To confirm the generation of dual-functionalities on the MXene surface, we performed microscopic and spectroscopic analyses on the prepared samples (Fig. 2). The magnified TEM image of Au@F-rich $Ti_3C_2T_x$ MXene illustrates high density of NPs without any aggregation or oxidation of the MXene substrate (Fig. 2a). The inset of Fig. 2a exhibits the fast Fourier transform (FFT) analysis of the MXene substrate. The selected area of few-layer MXene sheets shows lattice fringes of 0.265 nm, corresponding to the (01–10) plane of $Ti_3C_2T_x$.[36] X-ray photoelectron spectroscopy (XPS) analysis further confirms the low degree of oxidation (Fig. S7†). The Ti 2p peak of Au@F-rich $Ti_3C_2T_x$ MXene exhibits low peak intensity of TiO_2, indicating a low degree of MXene damage during the synthesis of the composite. Moreover, the synthesized Au NPs showed a uniform size distribution with an average particle size of 10.8 ± 3.2 nm on the MXene flakes (Fig. 2b). Such uniform size distribution is attributed to rapid heating and cooling of metal precursors during the fabrication of Au NPs, preventing the aggregation of individual nanoparticles.[31,33,37,38] The synthesized Au NPs were further confirmed by high resolution TEM (HRTEM) and the corresponding FFT analysis (Fig. 2c). The lattice distances of 0.238 nm and 0.144 nm correspond to the (111) and (220) lattices of the face-centered cubic (FCC) Au structure.[12] The XRD patterns of Au NPs synthesized by rapid Joule heating also correspond to the lattice spacing from FFT analysis (Fig. S8†). The amount of Au in the Au@F-rich $Ti_3C_2T_x$ MXene structure was 10.2 wt%, as measured by inductively coupled plasma mass spectrometry (ICP-MS).

Furthermore, the –F terminations on surface-termination controlled $Ti_3C_2T_x$ MXenes were compared using XPS analysis. The F 1 s XPS spectra of Au@F-rich $Ti_3C_2T_x$ still show a higher level of fluorine content compared to Au@ $Ti_3C_2T_x$ (Fig. 2d and e). The higher content of fluorine terminations in Au@F-rich $Ti_3C_2T_x$ is attributed to the synthesis step, where a higher proportion of HF was used for etching.[30] Although experimental studies have shown that fluorine terminations are removed during heating, the relatively retained level of –F terminations may be due to the very short duration of heating the sample undergoes.[39–41] The rich fluorine termination on the substrate surface and the fine distribution of Au NPs contribute to high cycle stability through uniform Li deposition and robust SEI layer formation, as we will discuss later in Fig. 3 and 4.

Fig. 3 shows the XPS depth profile analysis investigating the effect of F-termination on the SEI layer, highlighting the substantial impact of SEI components on battery performance. It is well-known that surface functionality plays a crucial role in the formation of the SEI layer, a critical factor influencing the performance of lithium-metal batteries. The SEI layer serves to prevent the further decomposition of the electrolyte and establish a stable interface for lithium-ion transport. However, it can also contribute to increased interfacial resistance and uneven lithium deposition, leading to capacity loss. Therefore, comprehending and regulating the formation and evolution of

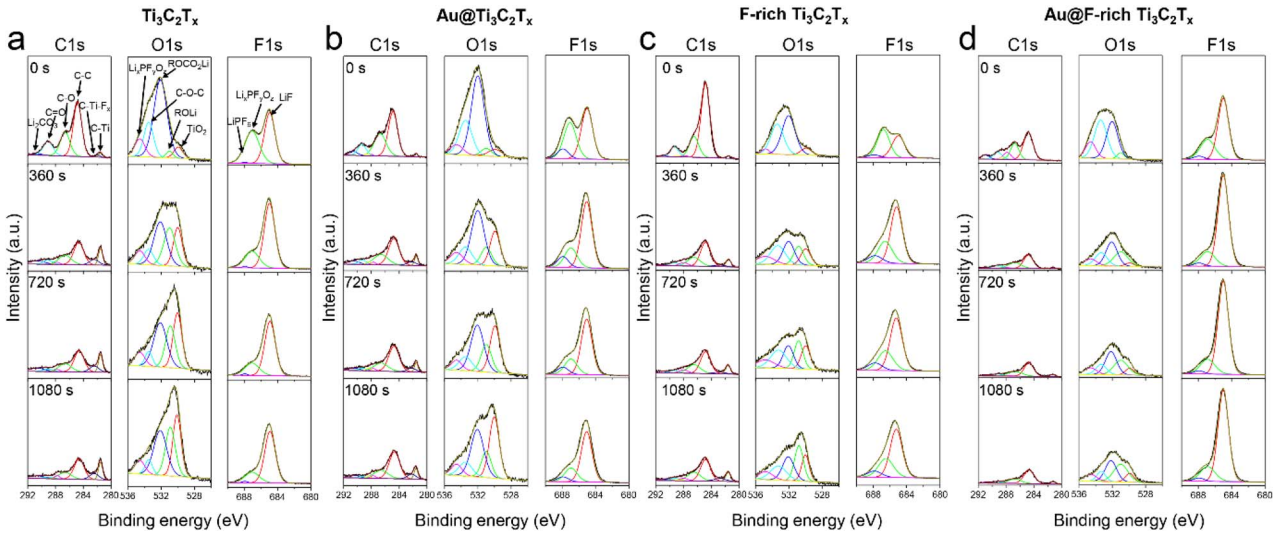

Fig. 3 XPS depth analysis of (a) $Ti_3C_2T_x$, (b) Au@$Ti_3C_2T_x$, (c) F-rich $Ti_3C_2T_x$ and (d) Au@F-rich $Ti_3C_2T_x$ after Li deposition of 0.1 mA h cm^{-2}.

Open Access Article. Published on 24 April 2025. Downloaded on 5/17/2026 5:31:30 AM.
This article is licensed under a Creative Commons Attribution-NonCommercial 3.0 Unported Licence.

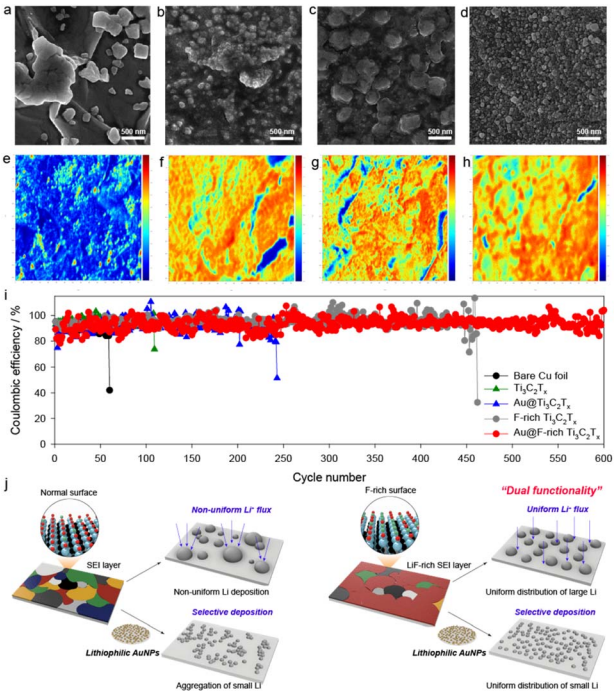

Fig. 4 Li deposition behavior and cyclic performance of MXene. SEM and SIMS images of (a) and (e) $Ti_3C_2T_x$, (b) and (f) Au@$Ti_3C_2T_x$, (c) and (g) F-rich $Ti_3C_2T_x$, (d) and (h) Au@F-rich $Ti_3C_2T_x$ and (e) $Ti_3C_2T_x$. (i) Cycle life of MXene at 1.0 mA cm^{-2}@1.0 mA h cm^{-2}. (j) Schematic illustration of Li deposition on MXene.

the SEI layer is essential for enhancing battery performance and longevity.

To elucidate the impact of MXene surface terminations on SEI components, four different samples with varying surface configurations were prepared: (i) $Ti_3C_2T_x$, (ii) Au@$Ti_3C_2T_x$, (iii) F-rich $Ti_3C_2T_x$, and (iv) Au@F-rich $Ti_3C_2T_x$. The XPS spectra of MXene substrates were acquired after Li deposition of 0.1 mA h cm^{-2}. In order to obtain the depth profiles of XPS spectra, argon-ion beam sputtering was performed for 0, 360, 720 and 1080 s. The C 1s spectra for all 4 samples contain peaks characteristic of C–Ti–F_x (282.7 eV) and C–Ti (281.9 eV) along with superimposed peaks including C–C (284.8 eV), C–O (286.5 eV), C=O (289.2 eV) and Li_2CO_3 (290.5 eV).[42,43] However, the peaks of C–Ti–F_x and C–Ti in the normal $Ti_3C_2T_x$ MXene samples ($Ti_3C_2T_x$, Au@ $Ti_3C_2T_x$) show relatively higher intensity than those in the F-rich $Ti_3C_2T_x$ MXene samples (F-rich $Ti_3C_2T_x$, Au@F-rich $Ti_3C_2T_x$) at the inner layers (360, 720, and 1080 s) as well as at the outermost layer.[44] This difference illustrates that the surface of the normal $Ti_3C_2T_x$ MXene samples is not robustly covered with the SEI layer, since the SEI layer on the normal $Ti_3C_2T_x$ MXene samples is not firmly formed and is relatively thin. Whereas it is suggested that the F-rich $Ti_3C_2T_x$ MXene samples have comparatively uniform and thick SEI layer.

Particularly, the peaks of C–Ti–F_x and C–Ti on the Au@F-rich $Ti_3C_2T_x$ exhibit relatively low intensity as the sputtering time is increased, suggesting that the SEI layer is most securely formed on the Au@F-rich $Ti_3C_2T_x$ sample. This interpretation is further clarified through the O 1s spectra. The intensity of the TiO_2 peak (529.9 eV), representing MXene, in the F-rich $Ti_3C_2T_x$ samples remains consistently low from the outer layer to the inner layer.[44] Alternatively, a broad peak centered at around 532 eV, which is assigned to a combination of $ROCO_2Li$ (532.0 eV), C–O–C (533.4 eV), $Li_xPF_yO_z$ (534.6 eV) and ROLi (531.0 eV) is more dominant in all spectra.[43] In contrast, normal $Ti_3C_2T_x$ MXene samples show higher intensity of the TiO_2 peak in all spectra. In particular, the intensity of the TiO_2 peak sharply increases in the spectra after a sputtering time of 360 s. This observation is consistent with the C 1s spectra, suggesting that the F-rich $Ti_3C_2T_x$ MXene samples, especially the Au@F-rich $Ti_3C_2T_x$, have a well-formed SEI layer. Meanwhile, the C 1s, O 1s and F 1s spectra indicate that the chemical composition of the SEI layer is not much different between the normal $Ti_3C_2T_x$ MXene samples and the F-rich $Ti_3C_2T_x$ MXene samples, including the Li_2CO_3, LiF, $ROCO_2Li$, RLi, $Li_xPF_yO_z$, *etc.* These chemical components of the SEI layer are well-known for facilitating the stable deposition and stripping of lithium metal. In particular, LiF, identified at 685.0 eV in the F 1s spectra, is considered a crucial component due to its favorable physical, chemical, and electrochemical properties.[45–47] The F 1s spectra indicate that the F-rich $Ti_3C_2T_x$ MXene samples, particularly the Au@F-rich $Ti_3C_2T_x$, exhibit a more pronounced LiF-dominant SEI with secure formation. In these samples, the intensity of LiF surpasses that of $Li_xPF_yO_z$ in all depth profiles. Conversely, the normal $Ti_3C_2T_x$ MXene samples display a more heterogeneous SEI composition, characterized by a mixture of LiF and $Li_xPF_yO_z$. The dominance of LiF in the SEI of the F-rich $Ti_3C_2T_x$ MXene samples can be attributed to the abundant F-termination on the surface, leading to the substantial formation of LiF components.

Generally, the presence of a LiF-rich SEI layer plays a significant role in enhancing the robustness and stability of the electrode, which in turn leads to considerable improvements in the electrochemical performance of the system. The LiF component within the SEI layer is known for its excellent chemical and electrochemical stability, protecting the lithium metal from degradation and minimizing side reactions during cycling. This LiF-rich SEI not only provides a physical barrier that prevents the direct contact of lithium with the electrolyte, but also promotes more stable and reversible lithium deposition and stripping, thereby improving cycle life and overall performance. As will be discussed in the following section, the excellent cycle stability of Au@F-rich $Ti_3C_2T_x$ is closely linked to the high concentration of LiF in its SEI layer. This well-formed LiF-rich SEI layer helps to maintain the integrity of the lithium surface throughout repeated cycling, reducing the formation of detrimental dendrites and minimizing the risk of capacity fade. As a result, the combination of high LiF content and a well-constructed SEI layer is crucial for ensuring long-term stability and high electrochemical performance, especially during extended charge–discharge cycles. This correlation strongly supports the idea that a well-formed LiF-rich SEI is key to enhancing the cycling stability of Au@F-rich $Ti_3C_2T_x$.

Fig. 4 shows the lithium deposition behavior and cyclic performance of the following samples: (i) $Ti_3C_2T_x$, (ii)

Open Access Article. Published on 24 April 2025. Downloaded on 5/17/2026 5:31:30 AM. This article is licensed under a Creative Commons Attribution-NonCommercial 3.0 Unported Licence.

Au@$Ti_3C_2T_x$, (iii) F-rich $Ti_3C_2T_x$, and (iv) Au@F-rich $Ti_3C_2T_x$. These samples were prepared and assembled into coin cells to demonstrate the impact of MXene surface terminations and the incorporation of Au NPs on reactivity with lithium, and specifically to observe which factor plays a greater role in performance. This approach enabled a comparative analysis to determine the relative significance of MXene surface terminations and the presence of Au NPs in affecting lithium reactivity and battery performance. Following the deposition of lithium at 1.0 mA h cm^{-2}, the cells were dissected, and the surface of each sample was examined using scanning electron microscopy (SEM). As shown in Fig. 4a, $Ti_3C_2T_x$ exhibited a non-uniform surface with lithium particles of varying sizes, ranging from hundreds of nanometers. Aggregation was evident on the $Ti_3C_2T_x$ surface, with portions exposed, demonstrating an uneven surface morphology after lithium deposition. Meanwhile, Au@$Ti_3C_2T_x$ displayed relatively smaller lithium deposits, suggesting that the introduction of Au NPs could reduce the size of deposited Li (Fig. 4b). However, aggregation was still observed, indicating that while Au NPs could influence deposited Li size, they may not completely eliminate aggregation. On the other hand, F-rich $Ti_3C_2T_x$ showed uniform lithium distribution without noticeable aggregation, emphasizing the role of F-termination in achieving a consistent lithium distribution (Fig. 4c). While F-termination did not significantly impact the size reduction of deposited Li, it played a crucial role in ensuring uniform Li distribution.

Fig. 4d illustrates Au@F-rich $Ti_3C_2T_x$, exhibiting small, uniformly distributed lithium particles. This indicates that the combined effects of Au, which reduces Li particle size, and F-termination, ensuring uniform distribution, contributed to the observed results. The SEM observations were correlated with secondary ion mass spectrometry (SIMS) analysis (Fig. 4e–h). The distribution of lithium concentration on the MXene surface was visualized through colored areas in SIMS images, with red areas indicating high concentration and blue areas indicating low concentration. Consistent with the SEM findings, Au@F-rich $Ti_3C_2T_x$ demonstrated the most uniform lithium distribution, reinforcing the advantages of Au NPs and F-termination in promoting uniform lithium deposition.

The electrochemical performances of the MXene samples were evaluated, as shown in Fig. 4i, at a current of 1.0 mA cm^{-2} and a capacity of 1.0 mA h cm^{-2}. Comparative analysis with the widely used Cu substrate for Li-metal battery anodes revealed that $Ti_3C_2T_x$ exhibited improved cycle performance, although with a limited lifespan of 100 cycles. Au@$Ti_3C_2T_x$ extended the lifespan to approximately 240 cycles, indicating the positive impact of Au NPs. F-rich $Ti_3C_2T_x$ outperformed the others with a lifespan of around 450 cycles, suggesting that F-termination yielded superior performance compared to the incorporation of Au NPs. Significantly, the Au@F-rich $Ti_3C_2T_x$ exhibited the most outstanding lifespan of 600 cycles, highlighting the critical role of the combination of Au NPs and F-termination in enhancing Li-metal battery performance, with F-termination proving to be a more significant factor than Au NPs. Such high stability of Au@F-rich $Ti_3C_2T_x$ outperforms previously reported Li-metal anodes with similar lithiophilic modifications (Table S1†). Although fluctuations are observed in Fig. 4i, long-term cycling stability is not compromised. These fluctuations are likely due to the extensive active surface area of the 3D structure and dynamic changes in the SEI layers. The corresponding current–time (i–t) and voltage–time (v–t) curves are provided as Fig. S9a and b.†

To examine charge–discharge behaviors of the substrates, the voltage profiles at 1.0 mA cm^{-2}@1.0 mA h cm^{-2} for bare Cu foil, $Ti_3C_2T_x$, Au@$Ti_3C_2T_x$, F-rich $Ti_3C_2T_x$, and Au@F-rich $Ti_3C_2T_x$ at selected cycles are shown in Fig. S10.† As shown, Au@F-rich $Ti_3C_2T_x$ exhibited the lowest overpotential and highest coulombic efficiency throughout cycling, demonstrating superior performance compared to the other substrates.

Additional tests were conducted at a current density of 5 mA cm^{-2} and a capacity of 3 mA h cm^{-2} and the results are shown in Fig. S11.† Under these conditions, the Au@F-rich $Ti_3C_2T_x$ exhibited the highest coulombic efficiency among MXene-based substrates, whereas the bare Cu foil did not function. However, compared to the performance at 1.0 mA cm^{-2} (Fig. 4i), the coulombic efficiency at 5 mA cm^{-2} was lower. This reduction in efficiency is in agreement with previous studies, which have shown that higher Li plating/stripping current densities compromise deposition uniformity and efficiency.[48–50] Despite this, the Au@F-rich $Ti_3C_2T_x$ substrate still outperforms other MXene-based substrates under high current conditions, demonstrating its potential for lithium-metal battery applications.

To observe initial electrochemical behaviors of the substrates, the first voltage profiles at current densities of 0.1 and 5 mA cm^{-2} for bare Cu foil, $Ti_3C_2T_x$, Au@$Ti_3C_2T_x$, F-rich $Ti_3C_2T_x$, and Au@F-rich $Ti_3C_2T_x$ are shown in Fig. S12.† Fig. S12a† shows the first Li plating voltage profiles at 0.1 mA cm^{-2}, where the presence of Au results in distinct profiles associated with lithium alloying, and the 3D architecture with a high surface area leads to sloping voltage profiles. In Fig. S12b,† Au@F-rich $Ti_3C_2T_x$ demonstrates the lowest overpotential and highest coulombic efficiency among the tested substrates, highlighting the excellent performance under high current density conditions.

Fig. 4j depicts schematic illustrations of lithium deposition behavior. A stable LiF-rich SEI layer formed by F-terminated $Ti_3C_2T_x$ promotes uniform Li^+ flux, while lithiophilic Au nanoseeds facilitate selective lithium deposition on the surface. Consequently, these surfaces serve dual functions, resulting in the uniform distribution of small lithium particles that effectively suppress dendritic lithium formation.

Furthermore, the stability of Au@F-rich $Ti_3C_2T_x$ was assessed by disassembling the cell after 600 cycles, and SEM images of the surface were examined. The results revealed a uniform surface with suppressed dendrite growth, attributed to the stable LiF-rich SEI layer and lithiophilic surface, as depicted in Fig. S13.† This confirms the long-term stability and durability of the proposed material configuration.

A full cell was constructed by assembling bare Cu foil and Au@F-rich $Ti_3C_2T_x$ with $LiNi_{0.8}Co_{0.1}Mn_{0.1}O_2$ (NCM811), and its cycle life was assessed, as shown in Fig. S14.† As depicted, the

Open Access Article. Published on 24 April 2025. Downloaded on 5/17/2026 5:31:30 AM.
This article is licensed under a Creative Commons Attribution-NonCommercial 3.0 Unported Licence.

capacity retention of the full cell utilizing bare Cu foil was 77.5% over 100 cycles, whereas the full cell employing Au@F-rich $Ti_3C_2T_x$ exhibited a capacity retention of 87.4%. Consequently, the superior cycling stability of Au@F-rich $Ti_3C_2T_x$ was clearly demonstrated.

Additional cycling tests without any pre-deposited Li on MXene were conducted and the results are shown in Fig. S15.† The cycling performances of five different samples were compared, and the Au@F-rich $Ti_3C_2T_x$ still demonstrated enhanced cycling stability relative to the other configurations. This result demonstrates that our dual-functional strategy—combining Au nanoseeds with abundant F terminations—not only promotes favorable SEI formation and uniform Li deposition under standard conditions but also remains effective under more rigorous conditions.

Conclusions

We have fabricated a high-density dual-functional surface for the first time, incorporating both lithiophilic metals and fluorine (–F) functional groups onto the anode substrate. Our study investigates the effects of surface termination and Au nanoparticles (Au NPs) on lithium deposition behavior and cycle performance of $Ti_3C_2T_x$ MXene as an anode material for lithium metal batteries (LMBs). Through a comprehensive analysis of morphology, structure, composition, and electrochemical performance in both half-cell and full-cell configurations, we have identified a significant synergy between Au NPs and F-termination. This synergy notably enhances the uniformity and stability of lithium deposition on $Ti_3C_2T_x$, resulting in improved cycling performance and safety of LMBs. Importantly, our findings underscore the critical role of F-termination compared to lithiophilic metal seeds such as Au NPs in extending the lifespan of Li-metal batteries. F-terminated $Ti_3C_2T_x$ promotes uniform lithium distribution by facilitating the formation of a solid electrolyte interphase (SEI) layer rich in LiF. This mechanism provides valuable insights for optimizing MXene-based substrates in the design of LMBs, emphasizing the importance of surface functionality and nanoseed tuning. Overall, our research proposes promising strategies for enhancing LMB performance and safety through tailored surface modifications in MXene materials.

Data availability

The data supporting this article have been included as part of the ESI.†

Author contributions

J. Yoon contributed to the conceptualization, investigation, electrode synthesis, and drafting of the original manuscript. O. B. Chae performed the formal analysis. M. Wu handled validation, methodology, and supervision. H.-T. Jung supervised the work and revised the manuscript. All authors have approved the final version of the manuscript.

Conflicts of interest

There are no conflicts to declare.

Acknowledgements

This research was supported by the National Research Foundation (NRF) of the Korean Government (NRF-2020M3H4A3081874, RS-2024-00337239 and RS-2021-NR057331) and the Semiconductor-Secondary Battery Interfacing Platform Technology Development Project of the NNFC.

References

1 W. Liu, D. Lin, A. Pei and Y. Cui, *J. Am. Chem. Soc.*, 2016, **138**, 15443–15450.
2 Q. Yun, Y. B. He, W. Lv, Y. Zhao, B. Li, F. Kang and Q. H. Yang, *Adv. Mater.*, 2016, **28**, 6932–6939.
3 M. S. Park, S. B. Ma, D. J. Lee, D. Im, S. G. Doo and O. Yamamoto, *Sci. Rep.*, 2014, **4**, 3815.
4 G. Zheng, S. W. Lee, Z. Liang, H. W. Lee, K. Yan, H. Yao, H. Wang, W. Li, S. Chu and Y. Cui, *Nat. Nanotechnol.*, 2014, **9**, 618–623.
5 K.-H. Chen, K. N. Wood, E. Kazyak, W. S. LePage, A. L. Davis, A. J. Sanchez and N. P. Dasgupta, *J. Mater. Chem. A*, 2017, **5**, 11671–11681.
6 J. Qian, W. A. Henderson, W. Xu, P. Bhattacharya, M. Engelhard, O. Borodin and J.-G. Zhang, *Nat. Commun.*, 2015, **6**, 6362.
7 R. Miao, J. Yang, Z. Xu, J. Wang, Y. Nuli and L. Sun, *Sci. Rep.*, 2016, **6**, 21771.
8 F. Zhao, P. Zhai, Y. Wei, Z. Yang, Q. Chen, J. Zuo, X. Gu and Y. Gong, *Advanced Science*, 2022, **9**, 2103930.
9 Y. Liu, Y. Li, J. Sun, Z. Du, X. Hu, J. Bi, C. Liu, W. Ai and Q. Yan, *Nano Research Energy*, 2023, **2**, e9120048.
10 Y. Liu, S. Xiong, J. Wang, X. Jiao, S. Li, C. Zhang, Z. Song and J. Song, *Energy Storage Mater.*, 2019, **19**, 24–30.
11 M. Chen, L. Cheng, J. Chen, Y. Zhou, J. Liang, S. Dong, M. Chen, X. Wang and H. Wang, *ACS Appl. Mater. Interfaces*, 2020, **12**, 3681–3687.
12 J.-Y. Song, J. Yoon, J. Suk, M. Wu and H.-T. Jung, *J. Mater. Chem. A*, 2023, **11**, 16153–16158.
13 C. Yang, Y. Yao, S. He, H. Xie, E. Hitz and L. Hu, *Adv. Mater.*, 2017, **29**, 1702714.
14 S.-S. Chi, Q. Wang, B. Han, C. Luo, Y. Jiang, J. Wang, C. Wang, Y. Yu and Y. Deng, *Nano Lett.*, 2020, **20**, 2724–2732.
15 Y. Jiang, J. Jiang, Z. Wang, M. Han, X. Liu, J. Yi, B. Zhao, X. Sun and J. Zhang, *Nano Energy*, 2020, **70**, 104504.
16 Y. Liu, S. Zhang, X. Qin, F. Kang, G. Chen and B. Li, *Nano Lett.*, 2019, **19**, 4601–4607.
17 F. Zhao, X. Zhou, W. Deng and Z. Liu, *Nano Energy*, 2019, **62**, 55–63.
18 K. Yan, Z. Lu, H.-W. Lee, F. Xiong, P.-C. Hsu, Y. Li, J. Zhao, S. Chu and Y. Cui, *Nat. Energy*, 2016, **1**, 16010.
19 D. S. Kim, Y. D. Yun, J. S. Kim, Y. B. Kim, S. H. Jung, N. G. Deshpande, H. S. Lee and H. K. Cho, *ACS Nano*, 2019, **13**, 5987–5998.

Open Access Article. Published on 24 April 2025. Downloaded on 5/17/2026 5:31:30 AM.
This article is licensed under a Creative Commons Attribution-NonCommercial 3.0 Unported Licence.

20 Z. Li, Y. Chen, X. Yun, P. Gao, C. Zheng and P. Xiao, *Adv. Funct. Mater.*, 2023, **33**, 2300502.
21 A. Jamaluddin, Y.-Y. Sin, E. Adhitama, A. Prayogi, Y.-T. Wu, J.-K. Chang and C.-Y. Su, *Carbon*, 2022, **197**, 141–151.
22 M. Naguib, V. N. Mochalin, M. W. Barsoum and Y. Gogotsi, *Adv. Mater.*, 2014, **26**, 992–1005.
23 Y. Gogotsi and B. Anasori, *ACS Nano*, 2019, **13**, 8491–8494.
24 G. S. Gund, J. H. Park, R. Harpalsinh, M. Kota, J. H. Shin, T.-i. Kim, Y. Gogotsi and H. S. Park, *Joule*, 2019, **3**, 164–176.
25 Y. Tian, Y. An, C. Wei, B. Xi, S. Xiong, J. Feng and Y. Qian, *ACS Nano*, 2019, **13**, 11676–11685.
26 F. Ming, H. Liang, G. Huang, Z. Bayhan and H. N. Alshareef, *Adv. Mater.*, 2021, **33**, 2004039.
27 C. Shi, J. Huang, Z. Cen, T. Yi, S. Liu and R. Fu, *Carbon*, 2024, **217**, 118616.
28 M. Alhabeb, K. Maleski, B. Anasori, P. Lelyukh, L. Clark, S. Sin and Y. Gogotsi, *Chem. Mater.*, 2017, **29**, 7633–7644.
29 M. A. Hope, A. C. Forse, K. J. Griffith, M. R. Lukatskaya, M. Ghidiu, Y. Gogotsi and C. P. Grey, *Phys. Chem. Chem. Phys.*, 2016, **18**, 5099–5102.
30 M. Tang, J. Li, Y. Wang, W. Han, S. Xu, M. Lu, W. Zhang and H. Li, *Symmetry*, 2022, **14**, 2232.
31 J. Yoon, Y.-J. Kim, J.-Y. Song, A. Jamal, I. Gereige, C. Kim and H.-T. Jung, *J. Mater. Chem. A*, 2023, **11**, 22295–22303.
32 S. Huang and V. N. Mochalin, *Inorg. Chem.*, 2019, **58**, 1958–1966.
33 Y. Yao, Z. Huang, P. Xie, S. D. Lacey, R. J. Jacob, H. Xie, F. Chen, A. Nie, T. Pu, M. Rehwoldt, D. Yu, M. R. Zachariah, C. Wang, R. Shahbazian-Yassar, J. Li and L. Hu, *Science*, 2018, **359**, 1489–1494.
34 J.-Y. Song, C. Kim, M. Kim, K. M. Cho, I. Gereige, W.-B. Jung, H. Jeong and H.-T. Jung, *Sci. Adv.*, 2021, **7**, eabk2984.
35 G. Li, J. Sun, W. Hou, S. Jiang, Y. Huang and J. Geng, *Nat. Commun.*, 2016, **7**, 10601.
36 R. Liu and W. Li, *ACS Omega*, 2018, **3**, 2609–2617.
37 Z. Huang, Y. Yao, Z. Pang, Y. Yuan, T. Li, K. He, X. Hu, J. Cheng, W. Yao, Y. Liu, A. Nie, S. Sharifi-Asl, M. Cheng, B. Song, K. Amine, J. Lu, T. Li, L. Hu and R. Shahbazian-Yassar, *Nat. Commun.*, 2020, **11**, 6373.
38 W.-B. Jung, Y. J. Hong, J. Yoon, S. Moon, S. Choi, D. Y. Kim, J. Suk, O. B. Chae, M. Wu and H.-T. Jung, *Nano Express*, 2022, **3**, 025005.
39 J. Björk and J. Rosen, *Chem. Mater.*, 2021, **33**, 9108–9118.
40 I. Persson, L.-Å. Näslund, J. Halim, M. W. Barsoum, V. Darakchieva, J. Palisaitis, J. Rosen and P. O. Å. Persson, *2D Materials*, 2018, **5**, 015002.
41 I. Persson, J. Halim, H. Lind, T. W. Hansen, J. B. Wagner, L.-Å. Näslund, V. Darakchieva, J. Palisaitis, J. Rosen and P. O. Å. Persson, *Adv. Mater.*, 2019, **31**, 1805472.
42 R. Dedryvère, S. Leroy, H. Martinez, F. Blanchard, D. Lemordant and D. Gonbeau, *J. Phys. Chem. B*, 2006, **110**, 12986–12992.
43 H. Ota, Y. Sakata, A. Inoue and S. Yamaguchi, *J. Electrochem. Soc.*, 2004, **151**, A1659.
44 J. Halim, K. M. Cook, M. Naguib, P. Eklund, Y. Gogotsi, J. Rosen and M. W. Barsoum, *Appl. Surf. Sci.*, 2016, **362**, 406–417.
45 Y. Liu, X. Tao, Y. Wang, C. Jiang, C. Ma, O. Sheng, G. Lu and X. W. Lou, *Science*, 2022, **375**, 739–745.
46 X. Fan, X. Ji, F. Han, J. Yue, J. Chen, L. Chen, T. Deng, J. Jiang and C. Wang, *Sci. Adv.*, 2018, **4**, eaau9245.
47 M. Chen, J. Zheng, Y. Liu, O. Sheng, Z. Ju, G. Lu, T. Liu, Y. Wang, J. Nai, Q. Wang and X. Tao, *Adv. Funct. Mater.*, 2021, **31**, 2102228.
48 S. Rajendran, A. Sekar and J. Li, *Chem. Eng. J.*, 2024, **484**, 149515.
49 S. Rajendran, A. Sekar and J. Li, *Carbon*, 2023, **212**, 118174.
50 Y. Chen, A. Elangovan, D. Zeng, Y. Zhang, H. Ke, J. Li, Y. Sun and H. Cheng, *Adv. Funct. Mater.*, 2020, **30**, 1906444.

 This journal is © The Royal Society of Chemistry 2025